

# Fluctuating Equilibrium MRI

Shreyas S. Vasanaawala,\* John M. Pauly, and Dwight G. Nishimura

**A new fast, spectrally selective imaging method called fluctuating equilibrium magnetic resonance is presented. With all gradients refocussed over a repetition interval, certain phase schedules of radiofrequency excitation pulses produce an equilibrium magnetization that fluctuates from excitation to excitation, thus permitting simultaneous acquisition of several images with different contrast features. For example, lipid and water images can be rapidly acquired. The effective echo time can be adjusted using the flip angle, thus providing control over the  $T_2$  contribution to the contrast. Several applications of the technique are presented, including fast musculoskeletal, abdominal, breast, and brain imaging, in addition to MR angiography. A technique for combining lipid and water images generated with this sequence for angiography is described and other potential applications are suggested. Magn Reson Med 42:876–883, 1999. © 1999 Wiley-Liss, Inc.**

**Key words:** fast imaging; steady-state free precession;  $T_2$  contrast; musculoskeletal imaging; abdominal imaging; magnetic resonance angiography; lipid suppression; fluctuating equilibrium magnetic resonance; MRA; FEMR

Techniques refocussing all gradients over a repetition interval have long been employed in NMR (1). Such methods were imported to MRI over ten years ago (2,3,4,5,6), and have been referred to by various names, including steady-state free precession (SSFP) and true fast imaging with steady precession (true FISP). These methods permit fast imaging with high signal, but suffer from bands of signal loss in images due to  $B_0$  inhomogeneity (7). Additionally, refocussed techniques yield an undesirably intense lipid proton signal. A solution to these two shortcomings of refocussed imaging is the subject of this paper.

Briefly, the banding artifact described above can be exploited as a novel tissue contrast generation mechanism. In this paper, we show that with an appropriate choice of sequence repetition time, all spins within a certain band of resonance frequencies can be suppressed while all other spins yield high signal. Furthermore, certain phase cycles of the radiofrequency pulse modify this spectral profile, and produce an equilibrium magnetization that fluctuates periodically from excitation to excitation. Thus, multiple images are acquired simultaneously, each with a different tissue contrast. In particular, lipid and water can be resolved based on chemical shift differences. Because conventional lipid suppression techniques are incompatible with any SSFP sequence, new applications of steady-state techniques are possible with this method. Thus,

several clinical applications of the technique are demonstrated in this paper, including musculoskeletal applications, abdominal imaging, brain MR, breast imaging, and fast MR angiography.

## THEORY

A timing diagram for a standard SSFP is shown in Fig. 1. After every excitation, phase encode and readout, magnetization is completely rewound with refocussing gradients on each axis. Thus, coherences are maintained from excitation to excitation, resulting in high equilibrium signal. The off-resonance properties of the sequence depend upon the excitation flip angle, with relatively high flip angles giving a large passband and a narrow stopband (Fig. 2), whereas low flip angles produce a narrow passband and a wide stopband. The artificial bands mentioned in the introduction are a manifestation of the stopband. Note that the graphs in Fig. 2 show only one cycle of functions that are periodic with off-resonance frequency; longer repetition times yield greater magnetization precision, and hence, more oscillations of the equilibrium magnetization over a given off-resonance range. Thus, brief repetition times minimize banding artifacts from magnetic field inhomogeneity.

With appropriate flip angles and repetition times, the off-resonance stopband described above can be designed to include the resonance frequency of lipid protons, thus yielding a novel lipid suppression technique (Figs. 2–4). Unfortunately, the technique is highly sensitive to field inhomogeneity, since the stopband is rather narrow (approximately 40 Hz). Additionally, in the case of lipids, the classically predicted behavior differs from that obtained experimentally. In particular, the experimental stopband is even narrower than expected and the signal intensity has an unexpected peak at one edge of the stopband (Fig. 5). This is presumably due to decoupling of methyl and methylene protons, a well-known effect in fast spin echo (FSE) imaging (8,9,10). Thus, the narrower stopband exhibited experimentally demands unacceptably severe constraints on field homogeneity to ensure adequate lipid suppression.

In standard SSFP imaging, the RF phase increases linearly from excitation to excitation. Instead, now consider the equilibrium signal for a refocussed sequence with RF phase alternating between  $\psi_1$  and  $\psi_2$  from excitation to excitation. Let the off-resonance frequency be  $\omega$ , the sequence repetition time  $T_R$ , and assume a hard pulse excitation of duration  $\tau$  and RF amplitude  $B_1$ . Also, let  $R_x(\alpha)$ ,  $R_y(\alpha)$ , and  $R_z(\alpha)$  denote rotations of angle  $\alpha$  about the  $x$ -,  $y$ -, and  $z$ -axis, respectively. Define  $\delta = -\omega/\gamma$ ,  $\beta = -\gamma\tau$ ,  $\sqrt{B_1^2 + \delta^2}$ , and  $\theta = \arctan(B_1/\delta)$ . Also,  $R_r = \text{diag}(e^{-T_R/T_2}, e^{-T_R/T_2}, e^{-T_R/T_1})$  and  $R_R = \text{diag}(0, 0, 1 - e^{-T_R/T_1})$  are diagonal  $3 \times 3$  matrices. Then, with  $M_0$  the thermal equilibrium magnetization, the steady-state magnetization

Magnetic Resonance Systems Research Laboratory, Department of Electrical Engineering, Stanford University, Stanford, California.

Grant sponsors: GE Medical Systems; National Institutes of Health; Grant numbers: CA 50948; HL 39297; NS 29434.

\*Correspondence to: Shreyas S. Vasanaawala, Stanford University, Department of Electrical Engineering, Packard 063, 350 Serra Mall, Stanford, CA 94305-9510. E-mail: vasanaawala@stanford.edu

Received 8 June 1999; revised 26 August 1999; accepted 27 August 1999.

1999 ISMRM Young Investigators' I.I. Rabi Award Finalist.

© 1999 Wiley-Liss, Inc.

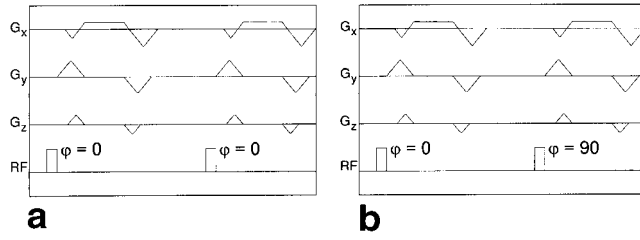


FIG. 1. Timing diagram for two-phase encoding steps of a 3D free precession sequence (a), and FEMR sequence with one phase encode repeated twice, but with two RF excitation phases (b). Both sequences employ a fractional echo.

just after the RF pulse with phase  $\psi_1$  is

$$M_1 = [R_z(-\psi_1)R_x(-\theta)R_z(-\beta)R_x(\theta)R_z(\psi_1) \\ - R_z(\omega T_R)R_rR_z(-\psi_2)R_x(-\theta)R_z(\beta)R_x(\theta)R_z(\psi_2)R_z(\omega T_R)R_r]^{-1} \\ \cdot [R_z(\omega T_R)R_rR_z(\psi_2)R_x(-\theta)R_z(\beta)R_x(\theta)R_z(\psi_2)R_r + R_r]M_0. \quad [1]$$

Note that although  $\omega$  appears explicitly in the equation above, there is also an implicit dependence on off-resonance frequency, as seen in the expressions for  $\delta$ , and  $\beta$ , and  $\theta$ .

More generally, for a sequence with RF pulse phases cycling through  $\psi_1 - \psi_2 - \dots - \psi_n$ , the steady-state magnetization just after the RF pulse with phase  $\psi_1$  is:

$$M_+ = [(1 - \prod_{j=1}^n S(\omega, \theta_j, \beta_j, \psi_j))S'(\omega, \theta_1, \beta_1, \psi_1)^{-1}]^{-1} \\ \cdot [1 + \sum_{j=2}^n \prod_{k=n}^j S(\omega, \theta_k, \beta_k, \psi_k)]R_R M_0 \quad [2]$$

where  $S'(\omega, \theta, \beta, \psi) = R_z(-\psi)R_x(-\theta)R_z(\beta)R_x(\theta)R_z(\psi)$  describes the effect of RF excitation and  $S(\omega, \theta, \beta, \psi) = R_rR_z(\omega T_R)S'(\omega, \theta, \beta, \psi)$  denotes RF excitation, free precession, and relaxation. Note that the products have indices running in reverse order since matrix multiplication is not commutative.

The sequence with flip angles  $\beta_1$  and  $\beta_2$ , and RF phases 0 and  $\psi$  that optimally broadens the stopband is found by first explicitly determining the steady-state transverse magnetization just after the RF pulse with phase 0,  $M_{xy} = M_x + iM_y$ . For this purpose, assume RF pulses of infinitesimal duration. Then, denoting  $\phi = \omega T_R$ ,  $E_1 = e^{-T_R/T_1}$ , and  $E_2 = e^{-T_R/T_2}$ ,

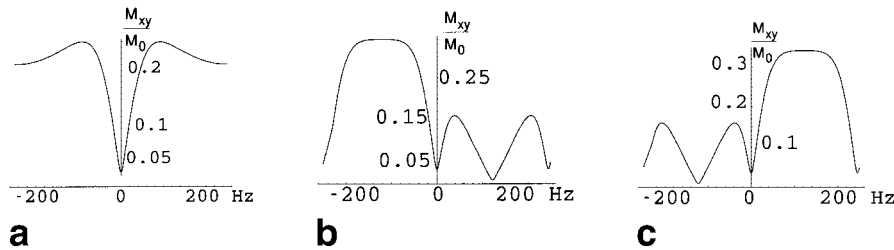


FIG. 2. Equilibrium transverse magnetization versus off-resonance for species with  $T_1$  of 170 msec and  $T_2$  of 40 msec. Graph a assumes a standard SSFP sequence with a 2.2 msec repetition time and 30° flip angle. Spins near the resonance frequency are suppressed, so by shifting the RF excitation frequency, a particular chemical species can be suppressed. Graphs b and c depict transverse magnetization just after the odd and even excitations, respectively, of a FEMR sequence with RF phase cycle of 0°–90°. Signal emanates alternatively from spins at 100 and –100 Hz relative to the RF excitation frequency. The width of the passband and stopband scale inversely with the sequence repetition time.

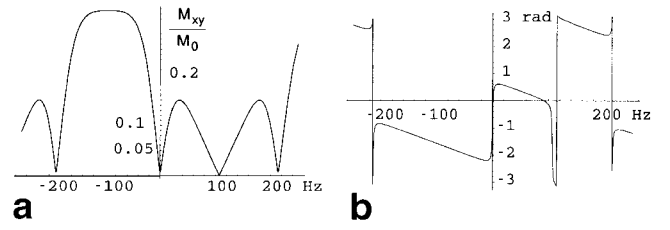


FIG. 3. Equilibrium transverse magnetization for a species with  $T_1$  of 900 msec and  $T_2$  of 200 msec just after even excitations from a 0°–90° FEMR sequence. a: Magnitude; b: graph phase. Note that the phase variation over the passband is relatively small, and hence causes minimal intravoxel dephasing.

$$M_{xy} = \frac{-i}{4} (-1 + E_1) e^{-i(\beta_1 + \beta_2 + 2(\phi + \psi))} \\ \cdot [4e^{i(\beta_2 + 2(\phi + \psi))}(-1 + e^{2i\beta_1}) + e^{i(\phi + \psi)}(-1 + e^{2i\beta_2}) \\ \cdot (e^{2i\psi}(-1 + e^{i\beta_1})^2 + e^{2i\phi}(1 + e^{i\beta_1})^2) \\ \cdot E_2 + (-1 + e^{2i\beta_1})(e^{2i\phi}(-1 + e^{i\beta_2})^2 - e^{2i\psi}(1 + e^{i\beta_2})^2) \\ \cdot E_2^2 - 2e^{i(\phi + \psi)}(1 + e^{2i\beta_1})(-1 + e^{2i\beta_2}) \\ \cdot E_2^3 + E_1[2e^{2i(\phi + \psi)}(-1 + e^{2i\beta_1})(1 + e^{2i\beta_2}) \\ + e^{i(\phi + \psi)}(-1 + e^{2i\beta_2}) \\ \cdot (-(e^{2i\psi}(-1 + e^{i\beta_1})^2) + e^{2i\phi}(1 + e^{i\beta_1})^2) \\ \cdot E_2 + (-1 + e^{2i\beta_1})(-(e^{2i\phi}(-1 + e^{i\beta_2})^2) \\ - e^{2i\psi}(1 + e^{i\beta_2})^2) \\ \cdot E_2^2 - 4e^{i(\beta_1 + \phi + \psi)}(-1 + e^{2i\beta_2})E_2^3]] \\ \div [-2 + 2E_1^2E_2^4 + (E_1^2 - E_2^2) \cos(\beta_1 - \beta_2) + (E_1^2 - E_2^4) \\ \cdot \cos(\beta_1 + \beta_2) + 4E_2[-(-1 + E_1^2)E_2(\cos(\frac{\beta_1}{2})^2 \\ \cdot \cos(\frac{\beta_2}{2})^2 \cos(2\phi) \\ + \cos(2\psi) \sin(\frac{\beta_1}{2})^2 \sin(\frac{\beta_2}{2})^2)] \\ + E_1(-1 + E_2^2) \cos(\phi) \cos(\psi) \sin(\beta_1) \sin(\beta_2)]] \quad [3]$$

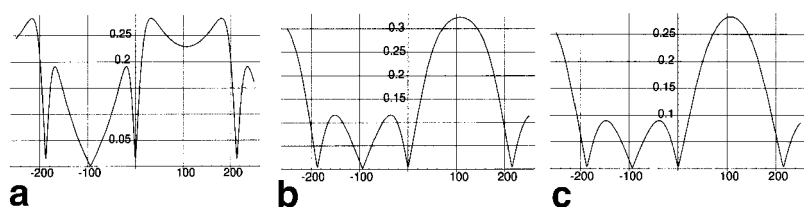


FIG. 4. Transverse magnetization ( $M_0 = 1$ ) as a function of off-resonance (Hz) for a FEMR sequence with flip angles of 15° (a), 45° (b), and 60° (c).

From the above equation, the sequence with two excitation pulses optimally broadening the stopband can be found numerically to have an RF phase cycle  $0^\circ$ – $90^\circ$  and equal flip angles for the two pulses. With this phase cycle, the equilibrium magnetization fluctuates between two profiles from excitation to excitation, as shown in Fig. 2. An analogous solution with  $0^\circ$ – $180^\circ$ – $180^\circ$ – $0^\circ$  phase cycle has similar equilibrium behavior of the magnetization magnitude, and the approach to steady state for both of these sequences is shown in Fig. 6. Establishing equilibrium requires many RF pulses, prolonging the imaging time, though, similar to SSFP (11), the magnetization oscillations can be significantly reduced in a  $0^\circ$ – $90^\circ$  sequence by halving the first two flip angles (not shown).

Note that the equilibrium transverse magnetization after the even and odd excitations in a  $0^\circ$ – $90^\circ$  sequence have off-resonance profiles nearly orthogonal; hence, two images can be simultaneously acquired by parsing data from even excitations to form one image, and from odd excitations to form another. Each image then represents spins in a different resonant frequency range, although there is some overlap since the stopband is not perfect. We will refer to this method as fluctuating equilibrium magnetic resonance (FEMR).

As a natural application of the  $0^\circ$ – $90^\circ$  schedule, water and lipid images with  $T_2$ -like weighting can be simultaneously and rapidly obtained. The frequency of the RF excitation pulse must be midway between the Larmor frequencies of water and lipid. Then with a sequence repetition time of 2.2 msec, the centers of the passband and stopband of the off-resonance profile will be separated by 220 Hz and will coincide with the Larmor frequencies of water and lipid at 1.5 T. The lipid and water images are perfectly registered since their phase encode acquisitions are interleaved.

The lipid image can be used to form a mask to suppress the display of the remaining lipid in the predominantly water image. Specifically, all pixels in the water image corresponding to the high intensity pixels in the lipid image are set to zero. Though this technique may introduce artifacts when voxels contain both water and lipid spins, it may be used to advantage in applications involving maximum intensity projections, such as MR angiography. Subtracting the lipid and water images is an alternative.

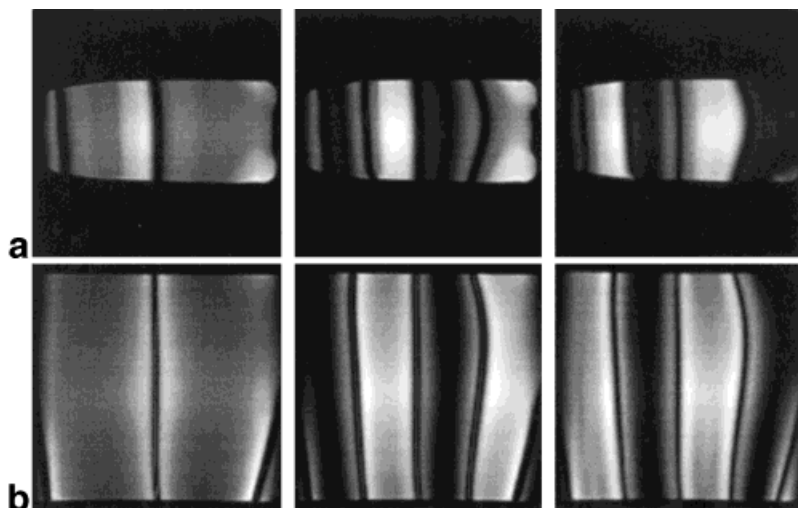
FEMR yields contrast based on a combination of  $T_1$  and  $T_2$ , with the relative  $T_2$  contribution controlled by changing the flip angle. Figure 7 shows equilibrium magnetization for a number of flip angles and values of  $T_1$ ; species with long  $T_2$  and short  $T_1$  yield high signal. For a given  $T_1$ , an effective echo time can be calculated, as shown in Fig. 8.

## EXPERIMENTAL TECHNIQUES

All experiments were conducted with a GE Signa 1.5-T scanner with gradient limits of  $|G| \leq 40$  mT/m and  $|dG/dt| \leq 150$  T/m/sec. Both two-dimensional (2D) FT and three-dimensional (3D) FT versions of SSFP and 0–90 FEMR sequences were implemented (Fig. 1 shows 3D FT version). The FEMR sequences were created by modifying SSFP sequences to give the appropriate RF phase cycle. Additionally, each phase encoding step is repeated twice and the data acquired after the odd and even excitations are parsed and reconstructed separately to generate two images. Because short repetition times are essential, a fractional echo capability with homodyne reconstruction was implemented. For the 2D FT sequence, 496  $\mu$ sec SLR excitation pulses were designed, whereas 160  $\mu$ sec hard pulses were employed in the 3D FT sequences.

To ascertain the off-resonance behavior of the SSFP and FEMR sequences, 2D images and field maps of uniform CuCl-doped water and lipid (soybean oil) phantoms were

FIG. 5. Axial images of lipid (a) and water (b) phantoms acquired with a shim gradient field running from the left to the right of each image. Left images were acquired with a 2D FT SSFP sequence, and the center and right images were acquired with a 2D FT FEMR sequence with a 0–90 phase cycle. For both sequences, a 45° excitation and 3.3 msec repetition time were employed. Note the relatively thin band of suppression with SSFP (left images) and a broad region of high intensity to the left of it. This pattern, lacking in the water image, may be due to decoupling of methyl and methylene protons in lipid, and the consequent increase in  $T_2$  relaxation time. However, the FEMR-acquired images have much broader bands of signal suppression, as predicted by theoretical off-resonance equilibrium magnetization profiles.



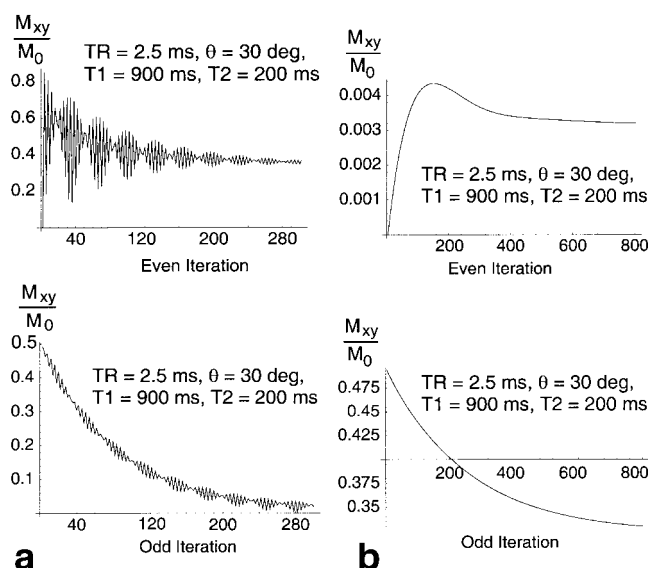


FIG. 6. Time evolution of  $M_{xy}$  from excitation to excitation with 0°-90° (100 Hz off-resonance, **a**) and 0°-180°-180°-0° phase cycles (zero Hz off-resonance, **b**). The upper graphs show  $M_{xy}$  immediately after even excitations, whereas the lower graphs show  $M_{xy}$  after odd excitations. The two phase schemes exhibit identical equilibrium behavior, but the 0°-90° cycle reaches equilibrium in about one second, whereas the 0°-180°-180°-0° cycle requires approximately 4 sec.

acquired with a shim field gradient applied in one direction. The water phantom had relaxation parameters of  $T_1 = T_2 = 82$  msec, and the lipid phantom had parameters of  $T_1 = 165$  msec and  $T_2 = 37$  msec. The shim gradient has constant magnitude throughout the scan, producing a spatially varying off-resonance. Registering the images with the field maps then permits assessment of the transverse magnetization of spins with a given resonance frequency.

To determine the feasibility of lipid suppression with FEMR in various anatomical regions, 2D FT or 3D FT implementations were used to image the knee, foot, brain, abdomen, and breast. In all cases, a 60% fractional echo and the shortest feasible repetition time was employed. Although 2.2 msec is ideal, the shortest achievable repetition time was 2.62 msec for the 2D FT sequence and 2.52 msec for the 3D sequence. Additionally, the center frequency for the scan was placed midway between water and lipid. To determine whether masking (as described in the

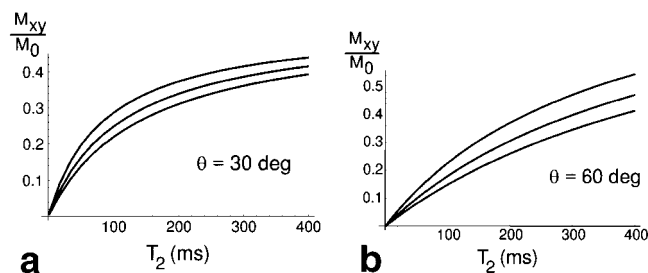


FIG. 7. Signal versus  $T_2$  for a 0°-90° FEMR sequence with repetition time of 2.5 msec and two flip angles of 30° (**a**) and 60° (**b**). From top to bottom, the curves are for species with  $T_1$  of 600, 800, and 1000 msec.

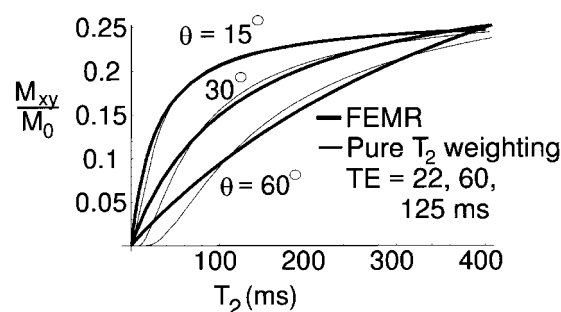


FIG. 8. The effect of flip angle on the contribution of  $T_2$  to contrast. The thicker curves show the equilibrium signal for a species with  $T_1$  of 800 msec for flip angles of 15°, 30°, and 60°. The thinner curves are best fits of  $\alpha \exp(-TE/T_2)$  with a TE of 22, 60, and 125 msec. Thus, for any given  $T_1$ , greater  $T_2$ -like weighting is achieved by higher flip angles.

previous section) improves lipid suppression, masked images of the knee were generated and angiograms of the popliteal artery were constructed from this image set with a maximum intensity projection algorithm.

## RESULTS

Figures 9 and 10 depict the spectral behavior of SSFP and FEMR sequences. Although results with water phantoms match theoretical calculations, lipid phantoms show a band of intense signal unanticipated by the Bloch equations. As mentioned above, this may be due to spin decoupling between various protons in lipids. However, a suppression band is still present in the lipid images, one broad enough to permit adequate lipid suppression in several applications.

A fast 3D technique with lipid suppression and bright synovial fluid is ideal for musculoskeletal applications, especially for rapid survey of large volumes. Figures 11 and 12 show just two examples. Note the low image intensity in regions of bone marrow and subcutaneous fat in the water images. The rapid scan time (84 sec) for these images compares favorably with conventional 3D techniques (12).

Another application of FEMR is fast brain imaging, with  $T_2$ -like weighting for gray/white matter discrimination and assessment of ventricles. In under 3 min, the entire head is imaged at  $1.1 \times 1.1 \times 2$  mm<sup>3</sup> resolutions with high SNR and bright cerebrospinal fluid (Fig. 13). Similarly, abdominal imaging benefits from a lipid-differentiated, high-SNR sequence fast enough to permit coverage of large anatomic regions within typical breathhold times (Fig. 14). Additionally, since the 2D method employs sequential acquisition of image slices, resumption of breathing towards the end of a scan corrupts only the final few images, in contradistinction to sequences such as FSE. Lipid-water discrimination is also valuable in breast imaging (Fig. 15).

Because the arterial blood  $T_2$  relaxation of 220 msec (13) is a relatively long compared with that of muscle, connective tissue, and venous blood (35, 35, and 100 msec, respectively), a novel type of flow-independent angiography is possible with FEMR. A large 3D volume can be rapidly imaged at high resolution, without administering a contrast agent. Figure 16 shows the feasibility of this



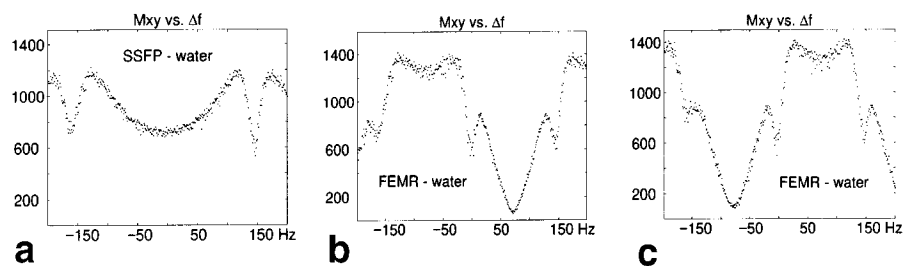


FIG. 9. Experimental determination of off-resonance behavior of  $0^\circ$ – $180^\circ$  SSFP and  $0^\circ$ – $90^\circ$  FEMR sequences with a repetition time of 3.3 msec. A water phantom with  $T_1$  and  $T_2$  of 82 msec was imaged with both sequences while a shim gradient was applied to generate a spectrum of off-resonance spins. Registering a field map with the acquired images permits determination of equilibrium transverse magnetization as a function of off-resonance, as shown above (a, SSFP; b, FEMR odd excitations; c, FEMR even excitations). With a repetition time of 3.3 msec, the transverse magnetization as a function of off-resonance is periodic with a period of 300 Hz. The vertical scale is arbitrary.

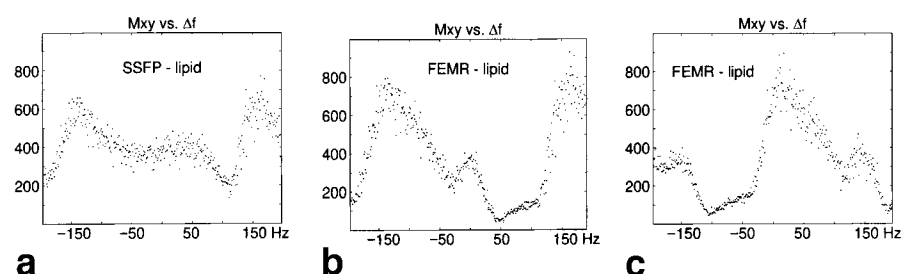


FIG. 10. Experimental determination of off-resonance behavior of  $0$ – $180$  SSFP and  $0$ – $90$  FEMR sequences with repetition time of 3.3 msec. A lipid phantom (soybean oil) with  $T_1$  of 165 msec and  $T_2$  of 37 msec imaged with both sequences while a shim gradient was applied to generate a spectrum of off-resonance spins. Registering a field map with the acquired images permits determination of equilibrium transverse magnetization as a function of off-resonance (a, SSFP; b, FEMR odd excitations; c, FEMR even excitations). With a repetition time of 3.3 msec, the transverse magnetization as a function of off-resonance is periodic with a period of 300 Hz. The vertical scale is arbitrary.

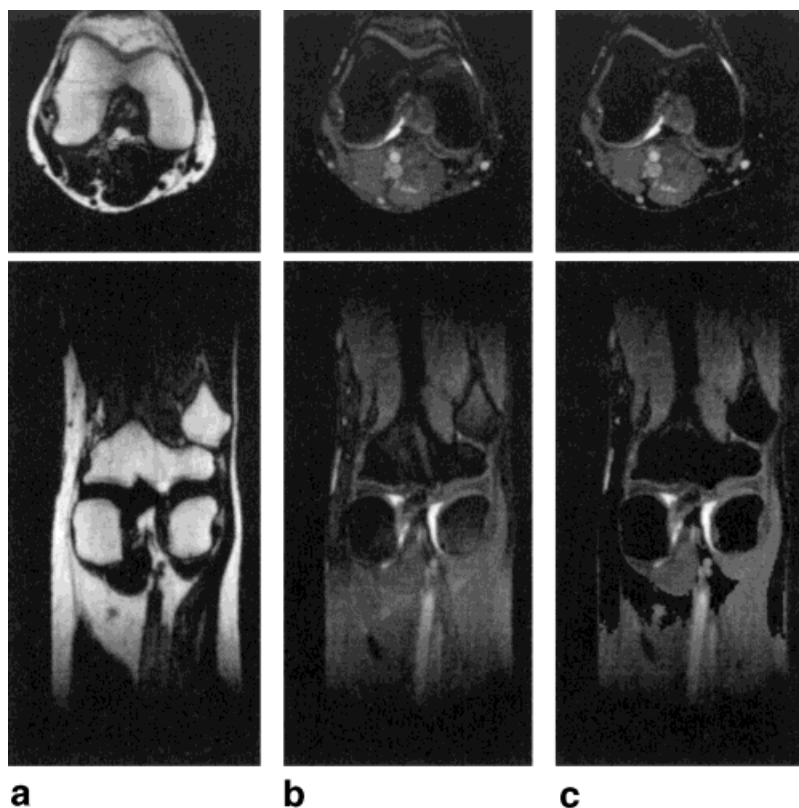


FIG. 11. Axial and coronal images from a 3DFT knee scan using  $0^\circ$ – $90^\circ$  FEMR with a  $26^\circ$  and a 60% fractional echo. Images in a show predominantly fat, while the simultaneously acquired images in b are mainly water. c: Water images masked with the fat images, and show very minimal fat. Synovial fluid and cartilage have high and intermediate signal intensities, respectively, on water images, whereas bone marrow and subcutaneous fat are bright in the lipid images. A total imaging time for  $28 \times 14 \times 14$  cm<sup>3</sup> FOV with 1.1-mm isotropic resolution of 84 sec yields both lipid and water images.

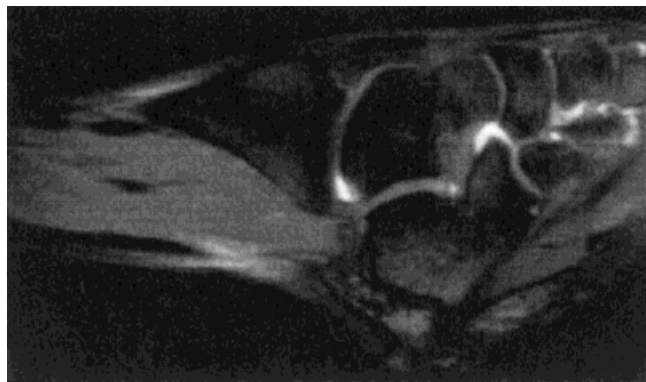


FIG. 12. Cropped sagittal image of the right foot acquired with a 3D FEMR sequence: 1.1 mm isotropic resolution.

method. Because lipid images with high SNR are also obtained, atherosclerotic plaque studies may also be possible.

## DISCUSSION

We have presented a method of incorporating water/lipid discrimination into refocused imaging sequences. Conventional lipid suppression methods, requiring large unrefocused gradients, inversion nulling, or length spectrally selective pulses, are incompatible with refocused imaging. Based upon the phantom studies, lipid suppression of approximately 85% can be achieved with FEMR. The quality

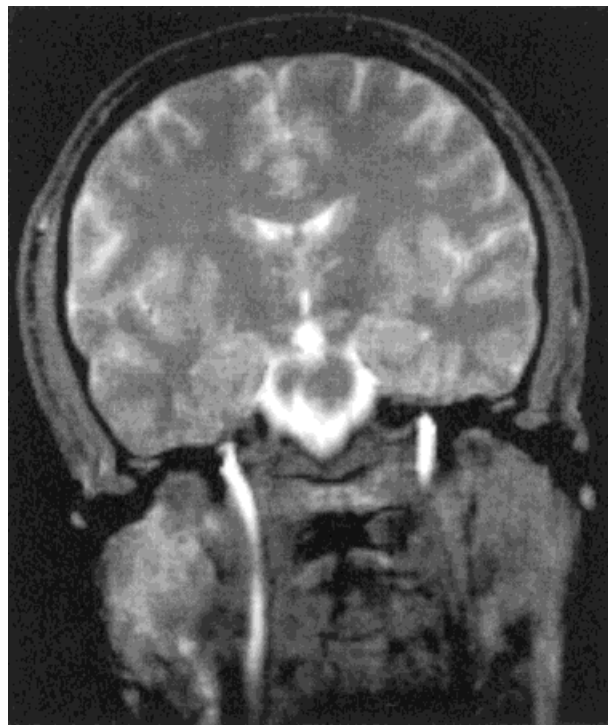


FIG. 13. Coronal slice of the brain obtained with a 3D FT FEMR sequence with 26° flip angle, 60% fractional echo,  $T_R = 2.52$  msec, and 0–90 phase cycle. Note the gray/white contrast, bright CSF signal, and delineation of the internal carotid arteries. The entire scan, covering  $28 \times 28 \times 28$  cm<sup>3</sup> with  $1.1 \times 1.1 \times 2$  mm<sup>3</sup> resolution, takes 2:45. No shimming was performed, and white matter has an SNR of 37, and gray matter 43.

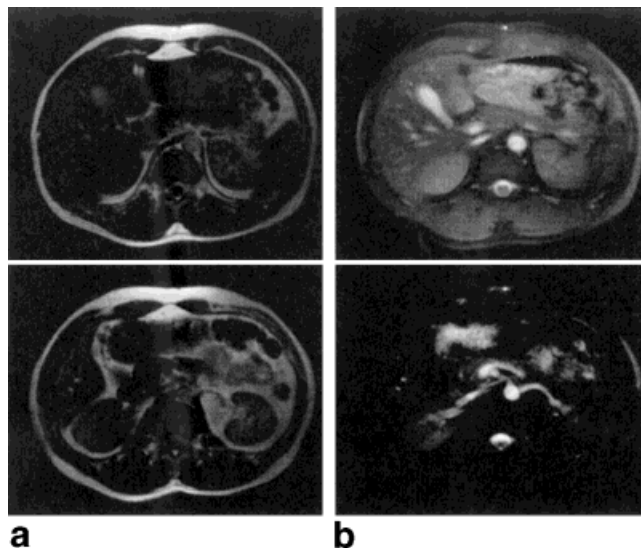


FIG. 14. Cropped axial fat (a) and water (b) images obtained with a 2D FT FEMR scan of the liver:  $36 \times 36$  cm<sup>2</sup> FOV with  $1.4 \times 1.4$  mm<sup>2</sup> resolution and 1 cm slice thickness; 45° SLR excitation pulse, 60% fractional echo, and a torso phased array coil were employed. The bottom water image is windowed to emphasize the renal artery. Seven slices were obtained in 11 with breathing suspended. Because the method sequentially acquires slices, sensitivity to suboptimal breath-holding is minimal, and no motion artifacts were discerned.

of in vivo lipid suppression in water images varies across the images due to field inhomogeneity, though the overall results are encouraging. Moreover, the availability of concomitant images with high lipid signal may improve the diagnostic utility of water images with suboptimal lipid suppression. The lipid/water suppression would be improved with faster gradients capable of a shorter repetition time, though even at the optimal repetition time of 2.2 msec, field inhomogeneity will remain an issue, potentially corrupting images.

For a comparison of SNR, assuming an effective echo time of  $TE = T_2$ , a 2D FSE sequence with enough interleaved slices for complete  $T_1$  recovery gives a signal of  $0.37 M_0$ ; for a species with  $T_1$  of 1000 msec and  $T_2$  of 50 msec, signal is about  $0.1 M_0$  with FEMR. Assuming equivalent voxel sizes and bandwidths, a 3D FEMR sequence yields greater SNR when fourteen or more slices are acquired. However, the scan time is significantly reduced; each slice-selective 180° pulse in FSE is approximately twice the entire repetition time for FEMR. Thus, even with double the number of excitations for lipid-water separation in FEMR, the scan time is approximately half. Thus, FEMR offers equal or higher SNR than 2D FSE in approximately half the scan time. Besides the shorter scan time and SNR advantage of FEMR over FSE, FEMR may offer superior image sharpness because the long echo train of FSE samples magnetization with variable  $T_2$  weighting. However, the contrast of FSE may be less dependent on  $T_1$ .

Additionally, species with a relatively high  $T_2/T_1$  ratio yield high signal. Thus, contrast-enhanced angiography is possible with this fast imaging method. Although angiograms can be obtained without contrast (Fig. 16), very low doses of gadolinium may be employed to further improve vessel contrast, permitting imaging at multiple stations without exceeding dosing guidelines. Assuming a  $T_1$  of

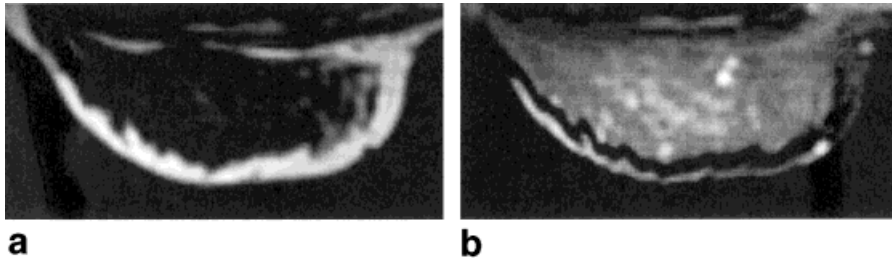


FIG. 15. Cropped axial fat (a) and water (b) images obtained with a 3D FT FEMR scan of the breast with a surface coil:  $28 \times 14 \times 14 \text{ cm}^3$  FOV with  $1.1 \times 1.1 \times 2.2 \text{ mm}^3$  resolution;  $26^\circ$  flip angle and 60% fractional echo were employed. Data was acquired in 1:30 with the volunteer prone and breathing freely.

1000 msec and  $T_2$  of 220 msec for blood at 1.5 T without contrast agent (14) and  $T_1$  of 800 msec and  $T_2$  of 35 msec for muscle (15), Fig. 17 shows the predicted signal and contrast achieved with Gd-DTPA using FEMR and a gradient-recalled steady-state sequence that rewinds phase encoding gradients. For a given concentration of contrast agent  $c$  with relaxivities  $r_1$  and  $r_2$ , enhanced relaxation times,  $T_1'$  and  $T_2'$ , for a species with  $T_1$  and  $T_2$  are given by

$$\frac{1}{T_1'} = \frac{1}{T_1} + cr_1 \quad \frac{1}{T_2'} = \frac{1}{T_2} + cr_2 \quad [4]$$

The relaxivities of Gd-DTPA are  $r_1 = 4.5 \text{ mmol L}^{-1} \cdot \text{sec}^{-1}$  and  $r_2 = 6.0 \text{ mmol L}^{-1} \cdot \text{sec}^{-1}$  at 0.5–1.5 T field strength

(16). The equilibrium magnetization for a FEMR sequence is given in the theory section, while the transverse magnetization for a gradient recalled steady-state sequence with flip angle  $\beta$ , according to Sekihara (17), is

$$M_y = \frac{M_0 \sin \beta}{1 + \cos \beta} \cdot \left( 1 - \frac{(e^{T_R/T_1} - \cos \beta) \sqrt{1 - e^{-2T_R/T_2}}}{\sqrt{(1 - e^{-T_R/T_1} \cos \beta)^2 - (e^{-T_R/T_1} - \cos \beta)^2 e^{-2T_R/T_2}}} \right) \quad [5]$$

Studies of contrast agent uptake kinetics are becoming more common in brain, breast, and abdominal imaging;

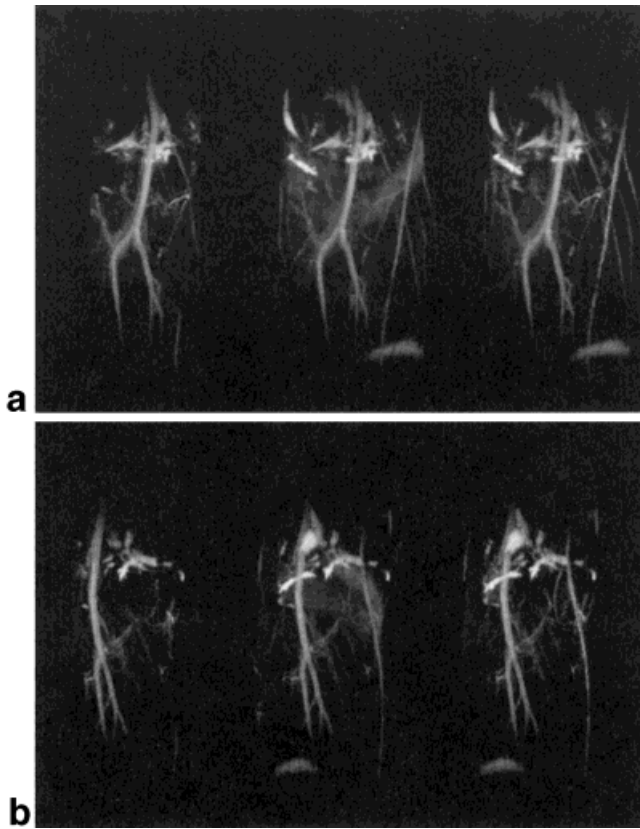


FIG. 16. Maximum intensity projections (MIP) of popliteal region. Images were obtained with a 3D FT FEMR sequence with  $T_R = 2.52$  msec,  $26^\circ$  flip angle, giving 1.1 mm isotropic resolution over  $28 \times 14 \times 14 \text{ cm}^3$  FOV in 84 sec. a: A projection from one viewing angle; b: projection from another angle. The left images are targeted MIPs of images with fat masking, so some superficial vessels and synovial fluid are eliminated. The middle images have no postprocessing, while the right images only have fat masking.

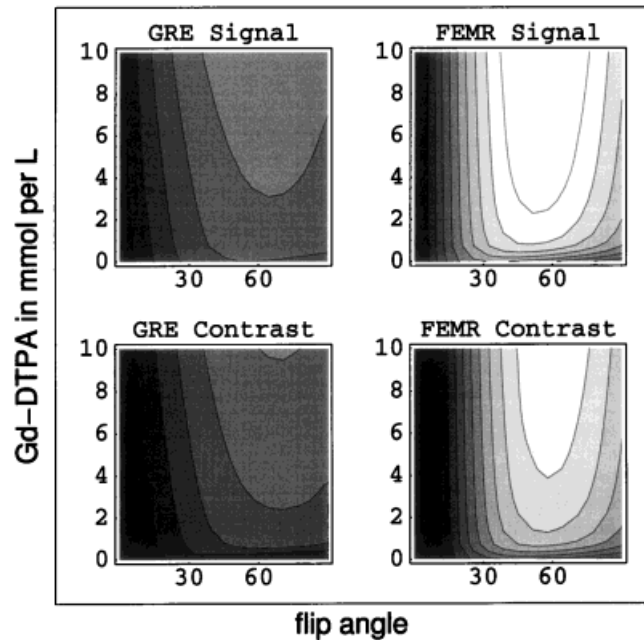


FIG. 17. Signal and contrast from blood vessels with Gd-DTPA against muscle. Contour plots of signal (top) and contrast (bottom) generated with a gradient-recalled steady-state sequence (left) and a  $0^\circ$ – $90^\circ$  FEMR sequence, both with repetition time of 2.5 msec. Lighter shades imply higher signal or contrast. Calculations assume  $T_1$  of 1000 msec and  $T_2$  of 220 msec for blood at 1.5 T without contrast agent and  $T_1$  of 800 msec and  $T_2$  of 35 msec for muscle; Gd-DTPA relaxivities of  $r_1 = 4.5 \text{ mmol L}^{-1} \cdot \text{sec}^{-1}$  and  $r_2 = 6.0 \text{ mmol L}^{-1} \cdot \text{sec}^{-1}$  were used. For reference, a single dose of Gd-DTPA distributed throughout the blood yields a concentration of about  $1 \text{ mm L}^{-1}$ . Note that higher signal and comparable contrast can be obtained with FEMR without contrast agent as can be obtained with high concentrations of gadolinium using standard sequences.



optimal use requires rapid injection and imaging, because equilibration between intravascular and interstitial spaces can be quick (18,19). Alternatively, fast  $T_2$ -weighted imaging with  $T_2$  shortening agents, such as superparamagnetic iron oxide may be useful.

The methods presented in this paper demand high gradient performance. Though a 2.2 msec repetition time provides optimal lipid/water separation, the shortest achievable repetition time with the system used in this study is 2.52 msec. Two alternatives may alleviate this issue. First, gradient heating constraints may be relaxed by forgoing collection of lipid echoes, though high gradient slew rates are still a prerequisite. Secondly, an alternative approach to refocussed imaging employing lower field strength has been advocated recently by Duerk et al. (20). For example, the optimal repetition time for water/lipid discrimination at 0.5 T is 6.6 msec, compared with 2.2 msec at 1.5 T. Of course, high-performance gradient systems are becoming more common and constantly improving. Thus, although the FEMR sequence is currently compatible with only short readout strategies, such as 2D FT, 3D FT, and projection reconstruction, future advances in gradient technology may permit spiral and echo planar  $k$ -space trajectories.

## CONCLUSION

Hence, FEMR is a novel, fast, high-signal, noninvasive imaging technique. With a fluctuating equilibrium magnetization, several images, each with different contrast, can be acquired simultaneously. Flexible control of the relative  $T_2$  contribution to contrast in images is achieved by varying the flip angle of RF excitation. Though very simple in concept and implementation, FEMR addresses the important problem of incorporating water/lipid discrimination into fast, high SNR refocussed techniques. In this paper we have demonstrated the feasibility of several natural applications: abdominal, musculoskeletal, brain, breast, and angiographic imaging.

## ACKNOWLEDGMENTS

Shreyas S. Vasanawala gratefully acknowledges the support of a Medical Scientist Training Program Scholarship.

## REFERENCES

1. Carr HY. Steady-state free precession in nuclear magnetic resonance. *Phys Rev* 1958;112:1693–1701.
2. Hinshaw WS. Image-formation by nuclear magnetic-resonance: sensitive point method. *J Appl Phys* 1976;47:3709–3721.
3. Mansfield P, Morris PG. In: *NMR imaging in biomedicine*. New York: Academic Press; 1982. p 65.
4. Oppelt A, Graumann R, Barfuss H, Fischer H, Hart W, Shajor W. FISP—a new fast MRI sequence. *Electromedica* 1986;54:15–18.
5. Hawkes RC, Patz S. Rapid Fourier imaging using steady-state free precession. *Magn Reson Med* 1987;4:9–23.
6. Jolesz FA, Patz S. Clinical experience with rapid 2DFT SSFP imaging at low field strength. *Magn Reson Imaging* 1988;6:397–403.
7. Zur Y, Stokar S, Bendel P. An analysis of fast imaging sequences with steady-state transverse magnetization refocussing. *Magn Reson Med* 1988;6:175–403.
8. Allerhand A. Analysis of Carr-Purcell spin-echo NMR experiments on multiple-spin systems. I. The effect of homonuclear coupling. *J Chem Phys* 1966;44:1–9.
9. Henkelman RM, Hardy PA, Bishop JE, Poon CS, Plewes DB. Why fat is bright in RARE and fast spin-echo imaging. *J Magn Reson Imaging* 1992;2:533–540.
10. Williamson DS, Mulkern RV, Jakob PD, Jolesz FA. Coherence transfer by isotropic mixing in Carr-Purcell-Meiboom-Gill imaging: implications for the bright fat phenomenon in fast spin-echo imaging. *Magn Reson Med* 1996;35:506–513.
11. Deimling M, Heid O. Magnetization prepared true FISP imaging. In: *Proceedings of the 2nd Annual Meeting of SMR*, San Francisco, 1994. p 495.
12. Disler DG, McCauley TR, Kelman CG, Fuchs MD, Ratner LM, Wirth CR, Hospodar PP. Fat-suppressed three-dimensional spoiled gradient-echo MR imaging of hyaline cartilage defects in the knee: comparison with standard mr imaging and arthroscopy. *Am J Roentgenol* 1996;167:127–132.
13. Wright GA, Hu BS, Macovski A. Estimating oxygen saturation of blood in vivo with MR imaging at 1.5 T. *J Magn Reson Imaging* 1991;1:275–283.
14. Wright GA. In: *Magnetic resonance relaxation behaviour of blood: study and applications*. PhD thesis, Stanford University, 1991.
15. Wright GA, Nishimura DG, Macovski A. Flow-independent magnetic resonance projection angiography. *Magn Reson Med* 1991;17:126–140.
16. Hendrick RE, Haacke EM. Basic physics MR contrast agents and maximization of image contrast. *J Magn Reson Imaging* 1993;3:137–148.
17. Sekihara K. Steady-state magnetizations in rapid NMR imaging using small flip angles and short repetition intervals. *IEEE Trans Med Imaging* 1987;6:157–164.
18. Hamm B, Wolf KJ, Felix R. Conventional and rapid MR imaging of the liver with Gd-DTPA. *Radiology* 1987;164:313–320.
19. Mirowitz S, Lee JKT, Gutierrez E, Brown JJ, Heiken JP, Eilenberg SS. Dynamic gadolinium-enhanced rapid acquisition spin-echo MR imaging of the liver. *Radiology* 1991;179:371–376.
20. Duerk JL, Lewin JS, Wendt M, Petersilge C. Remember true FISP? A high SNR near 1-second imaging method for T2-like contrast in interventional MRI at .2 T. *J Magn Reson Imaging* 1998;8:203–408.